An experimental evaluation of the accuracy to simulate granule bed compression using the discrete element method

Ann-Sofie Persson and Göran Frenning*

Uppsala University, Department of Pharmacy, Uppsala Biomedical Centre, P.O. Box 580, SE-751 23 Uppsala, Sweden.

*Corresponding author:
E-mail: Goran.Frenning@farmaci.uu.se, Fax +46 18-471 42 23, Phone +46 18-471 43 75

Abstract

In this work, granule compression is studied both experimentally and numerically with the overall objective of investigating the ability of the discrete element method (DEM) to accurately simulate confined granule bed compression. In the experiments, granules of microcrystalline cellulose (MCC) in the size range 200–710 μm were used as model material. Unconfined uniaxial compression of single granules was performed to determine granule properties such as the yield pressure and elastic modulus and compression profiles of the MCC granules were obtained from granule bed compression experiments. By utilizing the truncated Hertzian contact model for elastic-perfectly plastic materials, the rearrangement and plastic deformation stages of the force displacement curve were found to be in reasonable agreement with experiments. In an attempt to account for the final compression stage, elastic deformation of the compact, a simple modification of the contact model was proposed. This modification amounted to the introduction of a maximal plastic overlap, beyond which elastic deformation was the only deformation mode possible. Our results suggest that the proposed model provides an improved, although not perfect,

description of granule bed compression at high relative densities and hence may be used as a basis for future improvements.

Keywords: Compression, Discrete element method, Contact model, Plastic overlap, Elastic deformation

1. Introduction

Tablets are today the dominating dosage form available on the pharmaceutical market due to their safety and ease of administration. Compression of powders or granules (secondary particles) is however an intricate procedure. Confined compression of granular materials may typically be divided into a series of stages [1-3]. During initial compression, rearrangement of particles dominates with predominantly elastic particle deformation until a confined particle arrangement is reached and the motion is restrained. At increased pressure, the particles experience plastic deformation and possibly fragmentation that is followed by an elastic deformation of the compact. During the last stage of the compression cycle, unloading, the tablet first recovers elastically and may finally undergo an inelastic deformation at the end. Material properties such as plasticity, elasticity and contact forming ability are hence essential in order to manufacture a tablet with suitable mechanical properties.

By utilizing numerical simulations, an increased understanding of the mechanical properties that govern the compression process may be obtained. In addition, simulation may be a powerful tool in formulation development in order to predict compression properties. Numerical simulations may be based on either continuous or discrete models or a combination of both. The finite element method (FEM) is adopted for simulations at the continuum level and is typically used to

determine density and stress distributions within compacts of different shapes [4-7]. The FEM however requires indirect constitutive models for the powder behaviour that make predictions based on particle properties challenging.

The discrete element method (DEM), originally developed by Cundall and Strack [8], enables simulation at a microscopic level where the interparticle forces, particle velocities, etcetera, are calculated for each time step. Compression simulations of large systems comprising several thousand particles are possible using the DEM [9, 10]. In the DEM, the interparticle contacts are generally introduced as a function of the particle overlap and the contacts are typically assumed to be independent.

The FEM may be used for investigating local contact behaviours of powders during compaction when used in a combination with a micromechanical model [11]. The combined finite/discrete element (FE/DE) method gives a more thorough description of the particles during compression but is unfortunately also very time consuming. However, compression of plastically deforming granules has been investigated by the FE/DE method [12]. In order to save computational time when simulating contact forces, the extraction of a contact expression from the FE/DE method has proven successful in DEM simulations [13]. In order to simulate more realistic systems, corresponding to experimental compressions, the combined FE/DE method is impracticable. This and the simplicity of the DEM render the latter suitable for investigations of confined granule bed compressions and the DEM was therefore the focus of the current project.

DEM simulations have been used to investigate various powder compression processes. Both isostatic and closed die compressions have been performed to study particle rearrangement [14, 15] and the effect of size ratio in binary powder mixtures [9] and for frictionless spheres [10]. In addition, simulations of uniaxial compressions have previously been evaluated by experiments. By utilizing single granule mechanical properties, the potential of DEM simulations to accurately describe the bulk mechanical response has been proven [16-18].

During compression, the coordination number and contact area change with applied pressure. In order to enable simulations of granules, the formulation of a contact law between particles is critical. Various contact models have previously been derived, e.g. the models developed by Thornton and co-workers [19, 20] and Storåkers [21]. The choice of model is dependent on the material properties making the first suitable for elastic-perfectly plastic materials and the latter suitable for visco-elastic materials. As pharmaceutical materials most often display elastic-perfectly plastic behaviour the contact model developed by Thornton and Ning [20] is frequently utilized [16, 18]. The model accurately describes the initial particle rearrangement and the following plastic deformation. The model does however not depict the final elastic compact deformation and hence the contact model is not suitable for compressions at high relative densities. Before initiation of compression, the relative density of randomly close packed spheres is approximately 0.64 [22]. At increased compression pressure the interparticle contacts are independent up to relative densities of approximately 0.8. At higher relative densities, the contact deformation is dependent on the influence of neighbouring particles [14], which is not considered in the contact model. However, simulations at relative densities exceeding 0.8 are feasible using a

contact law derived from a combined discrete and continuum model in which Voronoi cells are used to estimate particle volumes [13].

In this work, granule bed compression was studied both experimentally and numerically with the general aim of investigating the ability of the DEM to accurate simulate confined granule compression. In order to match the experimental conditions, the properties of unconfined single granules composed of microcrystalline cellulose (MCC) were measured. In addition, granules of varying size were studied. In an attempt to account for the elastic deformation of the compact we propose a simple modification of the contact model for elastic-perfectly plastic materials. The modification amounts to the introduction of a maximal plastic overlap, where elastic deformation is initiated, in a similar manner as in a recent effective medium model of confined compression [23]. The simplicity of the modification was important in order to retain the computational efficiency of the original DEM and hence a perfect correlation to experimental data was not expected.

2. Theory

2.1 Original contact model

The normal contact force between two particles and between a particle and a confining surface was based on the model developed by Thornton and co-workers [19, 20]. The classical Hertz analysis is assumed to be valid before any plastic deformation has occurred. Hence the magnitude of the normal force (F_n) increases nonlinearly with normal overlap (δ_n), according to

$$F_n = \frac{4}{3} E_* R_*^{1/2} \delta_n^{3/2}, \quad (1)$$

where R_* and E_* are the effective radius and Young's modulus (see the Appendix). A limiting contact pressure P_y (henceforth referred to as the yield pressure) is introduced, such that plastic deformation commences once the maximal pressure in the contact region equals P_y. From the Hertz analysis if follows that plastic deformation starts at a normal overlap δ_y, calculated as

$$\delta_y = \left(\frac{\pi P_y}{2E_*} \right)^2 R_* . \tag{2}$$

This overlap corresponds to a normal force of magnitude $F_y = (4/3)E_* R_*^{1/2} \delta_y^{3/2}$, according to Eq. (1). The post-yield behaviour is inferred from a Hertzian contact pressure distribution that is truncated at P_y. As a result, the normal force increases linearly with the normal overlap during plastic loading,

$$F_n = F_y + \pi P_y R_* (\delta_n - \delta_y). \tag{3}$$

When unloading of plastically deformed particles takes place, the model accounts for plastic deformation by using a contact curvature $1/R_p$ that is smaller than $1/R_*$. The expression for the normal force becomes

$$F_n = \frac{4}{3} E_* R_p^{1/2} (\delta_n - \delta_p)^{3/2}, \tag{4}$$

where R_p and δ_p are parameters that depend on the amount of plastic loading. The parameter R_p is calculated as

$$R_p = \frac{F_e}{F_m} R_*, \tag{5}$$

where F_e is an equivalent normal force and F_m is the maximal normal force from which unloading starts. Specifically, if unloading starts from a maximal normal overlap δ_m, corresponding to a normal force F_m as inferred from Eq. (3), an equivalent elastic force F_e is

determined by using δ_m in Eq. (1). Finally, the parameter δ_p is determined from the condition that Eqs. (3) and (4) must produce the same normal force at a normal overlap of δ_m.

The tangential contact force between two particles and between a particle and a confining surface was based on the modification of the Mindlin–Deresiewicz model proposed by Di Renzo and Di Maio [24]. As long as no slip occurs, the magnitude of the tangential force (F_t) hence increases linearly with the tangential overlap (δ_t) with a constant of proportionality that depends on the normal overlap,

$$F_t = \frac{16}{3} G_* R_*^{1/2} \delta_n^{1/2} \delta_t , \tag{6}$$

where G_* is the reduced shear modulus (see the Appendix). The tangential force was truncated in accordance with Coulomb friction, using a sliding friction coefficient μ_s. In addition, rolling torques were included in the model, as proposed by Zhou et al. [25], with a rolling friction coefficient μ_r.

2.2 Modified normal force model

A shortcoming of the truncated Hertzian model in its original form is that it allows plastic deformation to continue indefinitely. This poses no problems in typical DEM analyses that entail limited particle overlap, but is unsatisfactory for simulations of powder compression, where the overlap becomes much larger. During confined compression, a porous particle may densify plastically, but plastic deformation must come to an end once the particle has become essentially nonporous. To account for this phenomenon in a simplified manner, a maximal plastic overlap was introduced, denoted by δ_e, beyond which elastic deformation was the only mode of deformation possible. Once δ_e was exceeded, the elastic unloading law, Eq. (4), was in effect

employed both during loading and unloading (with R_p and δ_p calculated from δ_e rather than δ_m). For contact between monosized spherical particles with radius R, δ_e may be estimated from the equation

$$\left(1-\frac{\delta_e}{R}\right)^3 = \eta\phi, \tag{7}$$

where η is the solid fraction of each particle (i.e., one minus the particle porosity) and ϕ is the filling fraction of a regular particle arrangement (such as the simple cubic lattice). The value of δ_e calculated by Eq. (7) pertains to contact between particles and confining surfaces, whereas the overlap for contact between two particles of the same type will be twice as large (since the deformation of each particle corresponds to half the overlap). A comparison between the predictions of the original and modified contact laws is presented in Sec. 4.2 below.

3. Materials and methods

3.1 Materials

Microcrystalline cellulose (MCC) spheroids of three size distributions (Cellets® 200 (200-355 µm), 350 (350-500 µm), and 500 (500-710 µm)) were purchased from HARKE Pharma GmbH, Germany. The granules are hereafter referred to as C200, C350, and C500, respectively. The apparent particle density, ρ_{app}, of MCC (number of independent measurements, n = 2) is 1.57 g/cm^3 (AccyPyc 1330, Micrometrics, USA). The granules were stored at 40 % relative humidity (over a saturated solution containing potassium carbonate) at room temperature for at least 5 days prior to use. Magnesium stearate (Kebo, Sweden) was used as lubricant.

3.2 Experimental methods

3.2.1 Granule properties

The median granule size was assessed by scanning the granules (n>1000) on a flatbed scanner (Epson Perfection 1640SU Scanner, Seiko Epson Corp., Japan). Images of 1600 dpi resolution were captured and analysed with ImageJ [26]. The granule diameter was calculated from the projected circle area assuming spherical particles.

The poured bulk density, ρ_{bulk}, (n=3) was assessed by weighing (Delta Range B3002, Mettler Toledo, Swizerland) 50 mL granules, which were poured through a funnel into a measuring cylinder (21.7 diameter). The granule bed was subjected to 1250 taps (PharmaTest, PT-TD, Hainburg, Germany) in order to assess the tapped bulk density, ρ_{tap}, (n=3) according to the European Pharmacopoeia [27].

Steady-state permeametry (n=3) was used to measure the granule volume specific surface area. The granules (~9-11 g) were manually poured into a cylinder (diameter 11.47 mm and height 150 mm) and the height was recorded (Mitutoyo Digimatic, ID-C, Tokyo, Japan). Air flow of controlled rate (Brook flow meter, Brook Instruments B. V., the Netherlands) was allowed through the granule bed. The build-up pressure was measured from high to low flow rate using a manometer (P 200 S, Digitron Instrumentation Ltd, UK) and was used for calculation of the granule external surface area as described earlier [28].

Low pressure mercury pycnometry (Autopore III 9420, Micrometrics, USA) was utilized for determination of the effective particle density, ρ_{eff}, (n=2) as described earlier [29]. The granules were stored over silica gel (RH ~23 %) at room temperature prior to the measurement to facilitate the degassing step. The porosity was calculated as one minus the ratio between the effective and apparent particle densities.

3.2.2 Mechanical properties of single granules

Unconfined uniaxial compressions of single granules (n=50) were performed using a Texture analyzer (TA.HDi Texture Analyser, Stable Micro Systems, UK) with a 5 kg load cell at a rate of 0.05 mm/s. Single granules were compressed between a flat surface and a cylindrical movable probe (6 mm diameter). The force required to fracture the granules, F_{frac}, was measured to enable calculations of granule tensile strength, σ_0, according to

$$\sigma_0 = \frac{4F_{frac}}{\pi d^2}, \tag{8}$$

where d is the granule diameter [18]. In addition, the E_* and the P_{y} was determined using the truncated Hertzian elastic correlation and the model of elastic-perfectly plastic contact deformation according to Eq. (1) and Eq. (3), respectively. By fitting Eqs. (1) and (3) to the single granule compression data, the Young's modulus and yield pressure were calculated by linear regression from the slopes of the respective force-displacement curves.

3.2.3 Confined granule bed compression

Granules (0.5 g) were compressed (n=5) in an uniaxial manner with a stationary lower punch and movable upper punch (diameter 11.3 mm) using a materials tester (Zwick Z100, Zwick/Roell GmbH & Co. KG, Ulm, Germany). A load of maximum 300 MPa was applied to the granule bed and the compressions were performed at a rate of 25 mm/min. The punches and die were lubricated using 1% magnesium stearate in ethanol before compression to reduce the particle-wall friction.

Prior to compression, punch deformation curves were obtained from pressing the lower and upper punch together. To account for the elastic deformation of the punches, Δ, the compression data was fitted to the equation $\Delta = l_a + k_a P + l_b e^{-k_b P}$, where the exponent describes an initial curvature at low compression pressure, P. The parameters l_a, k_a, l_b and k_b are determined from the fit and punch deformation was corrected for in the calculations of granule bed height [30].

3.2.4 The Kawakita model for description of porosity-pressure relationship

The equation developed by Kawakita and Lüdde was utilized to describe granule bed compression [31],

$$C = \frac{h_0 - h}{h_0} = \frac{abP}{1 + bP}, \qquad (9)$$

where C is the engineering strain, h_0 and h are the height of the granule bed before compression and at applied load, P, respectively. The Kawakita parameters a and b are constants describing material properties. The Kawakita constant a corresponds to C_{max} (maximal engineering strain) and represents the porosity of the granule bed at an early stage compaction. The reciprocal of b is a measure of the pressure required to reach a degree of compression of $a/2$.

The Kawakita Eq. (9), when expressed in the linear form

$$\frac{P}{C} = \frac{1}{ab} + \frac{P}{a}, \qquad (10)$$

enables the determination of the Kawakita parameters. The parameters were calculated by linear regression in a pressure range of 75-300 MPa with squared regression coefficients $R^2 > 0.999$.

3.3 Numerical methods

In order to obtain an as close correspondence as possible between experiments and simulations, the particle size, density and yield pressure were chosen to match the experimental values (see below). For simplicity, monodisperse particles were assumed, with sizes equal to the median values of the experimental particle-size distributions. The particle numbers (C200, 20 634; C350, 7585; C500, 2497) were inferred from the particle weight and the total weight of granules used in each compression (0.5 g). Since the effect of particle elasticity was expected to be most important towards the end of each granule bed compression for the modified model, the Young's modulus was set equal to 8 GPa, which was considered as a typical value for zero porosity compacts formed from MCC [32]. Poisson's ratio was set to 0.3 and representative values – that have previously been used in simulation of granule flow [33] – were selected for the sliding and rolling friction coefficient between particles (0.5 and 1 μm). Both the sliding and the rolling friction coefficients were assumed to be 5 times smaller for the particle–wall than for the particle–particle interaction. The maximal plastic overlap was estimated from Eq. (7), typically using filling fractions corresponding to the simple-cubic (SC) lattice with 6 nearest neighbours ($\phi_{\mathrm{SC}} = \pi/6 \approx 0.524$). In addition, the maximal plastic overlap was in some simulations based on a body-centred cubic (BCC) particle arrangement with 8 nearest neighbours ($\phi_{\mathrm{BCC}} = \pi\sqrt{3}/8 \approx 0.680$).

Initial particle assemblies were generated by letting randomly moving particles settle under the influence of gravity in a cylindrical die cavity of the same diameter as the one used in the experiments. Both normal and tangential contact damping were included in order to efficiently dissipate the kinetic energy of the particles. Three distinct initial particle assemblies were generated for each granule type.

Compression simulations were performed for each assembly, with the same punch speeds as in the experiments, using both the original and the modified contact models described in Sec. 2 above. Preliminary runs indicated that mass scaling may influence particle rearrangement somewhat during the early stages of compression; consequently no mass scaling was used during this stage. However, once a confined state was reached, at a coordination number of about 6, no adverse effects of mass scaling were seen. The particle mass was therefore artificially increased by a factor of 1000 once the coordination number exceeded a threshold value of 6. Loading proceeded until the height of the compact was 3.2 mm, similar to the height of the experimental compact. When the DEM is used, overlaps between all particles in contact are determined at each time step. The maximal value of these (henceforth referred to as the maximal particle overlap) was recorded and used as an indicator of the evolution of the compression process (in particular of the transition from plastic to elastic particle deformation).

4. Results and discussion

4.1 Experimental study

4.1.1 Granule characteristics

The measured size distributions (Fig. 1) were consistent with the specifications by the manufacturer (with $\geq$ 85% of the granules in the specified range). The median particle sizes (Table 1) were used in all calculations and simulations. The size distributions are the only difference between the granule types, which were equal regarding constituting material and porosity. Similar granule characteristics were hence expected and indeed obtained from the measurements (Table 1). The spherical shape and large particle size resulted in a close granule

packing when pouring, especially for the largest granules, and consequently the bulk density only increased to a small extent when the granule bed was subjected to tapping. The simplicity by which the granules are able to slide and roll past one another makes the granules pack closely, which is advantageous during the rearrangement process at the initial stage of granule bed compression.

The surface areas inversely reflected the particle sizes, the smaller the granules the larger the surface areas. Granules possessing large surface areas facilitate formation of numerous interparticle contacts during compression compared to larger granules, resulting in compacts of higher strength [34].

4.1.2 Compression properties of single granules

Compressions of 50 single granules were performed for each size distribution. At the beginning of loading the displacement increased non-linearly followed by a linear increase before a distinct drop or a flattening of the force-displacement curve appeared (Fig. 2). This peak was considered as the force required to fracture the granules, F_{frac}, and hence used for calculations of the single granule strength. As observed in Fig. 2, the deformation before fracture increased with particle size and thus higher forces were necessary to break the larger granules. Continuous loading deformed the granules further but rarely caused the granules to fracture once more. Data for single granule strength are presented in Table 2 and a significant difference ($p<0.05$) was found between C200 and C500 in σ_0 (as inferred from ANOVA followed by post hoc tests), implying that C200 granules were stronger than the C500.

As the granules possessed approximately equal and low porosity (Table 1), the deformation properties were expected to be similar for the different granules. Typical force-displacement curves for elastic-perfectly plastic materials involve a non-linear initial stage corresponding to Hertzian deformation that is followed by a linear part displaying the plastic deformation. The typical appearance is however difficult to detect from the force-displacement curves in Fig. 2. At initial loading the granules may have rotated into the most stable position, which renders the interpretation of the non-linear region somewhat uncertain. However, it likely corresponded to the Hertzian deformation that is followed by plastic deformation. The elasticity and plasticity were evaluated by determining the effective Young's modulus, E_*, and yield pressure, P_y, respectively. A significantly higher E_* was obtained for C350 compared to C200 whereas significant differences in P_y were obtained between all granule types, which displayed a size dependence in the initiation of plastic deformation. However, the large variations in mechanical properties imply some uncertainties in the elastic and plastic parameters for single granules. The values of E_* and P_y were consistent with published data for larger low porosity MCC granules [30], especially when the size dependence of these parameters is taken into account.

4.1.3 Compression properties of granule beds

The relationship between pressure and porosity/strain during granule bed compression in-die is usually described by various compression equations such as the Heckel [35] and the Kawakita [31] correlations. In this work, the Kawakita expression was utilized for describing the compression of MCC granules, as the equation previously has proven suitable for analysing compression of pharmaceutical granules [30].

Utilizing the Kawakita equation necessitates determination of the initial powder height in-die, h_0, since the initiation of compression is crucial for calculations of the engineering strain. In order to determine h_0 several methods are reported in the literature, e.g. h_0 may be calculated from the poured bulk density [30] and at a certain applied load [36]. A load of 1 MPa is reported suitable for powders but was in this work considered high for spherical granules and instead the height at an applied load of 0.5 MPa was chosen as h_0.

During compression, the granule beds behaved in a similar manner (Fig. 3a) resulting in a maximum engineering strain, C_{max}, of about 0.5, which is consistent with earlier compaction data of low porosity MCC granules [36].

Correlating bulk compression data to the Kawakita equation provided similar profiles for the various granules (Fig. 3b). At low compression pressure (<75 MPa) the curves were non-linear and at increasing load the relationship between P/C and P became linear. The reciprocal of the slope of the linear region provided the Kawakita parameter a, and the intercept gave the value of the reciprocal of ab (Table 3).

4.2 Numerical study

Simulations were performed with the original and the modified contact models described in Sec. 2 above. The predictions of these models are illustrated in Fig. 4a, which shows force–deformation curves for single granule compressions. The parameter values were selected to match the experimental C350 granules and, for the modified model, the maximal plastic overlap was based on the SC and the BCC lattice. All curves initially follow the same path, as expected, with limited elastic deformation and an extended plastic region, during which the normal force

increases linearly with the deformation. For the modified models, elastic deformation starts once the maximal plastic overlap is reached, resulting in a much more rapid increase in force than for the original model. In reality, the transition from plastic to elastic deformation would only be observed under confined conditions, since plastic deformation cannot account for any volume reduction past zero porosity. The particle has deformed plastically prior to the transition to elastic deformation and will thus retain a substantially changed shape upon unloading, during which, all models predict a purely elastic recovery.

The simulations with the original contact model (solid line in Fig. 4b) revealed as expected only an approximately linear increase in pressure with engineering strain, representing the plastic deformation of the granules. For simplicity, we will henceforth refer to this trajectory as linear, even though a slight curvature results from the increase in coordination number discussed below. In addition, a small elastic recovery of the compact was visible during unloading. For the modified contact models (dashed and dotted lines in Fig. 4b), the initial plastic deformation was the same as for the original model. At increased engineering strain, the curves started to deviate from linearity, which is a typical indication of the initiation of elastic compact deformation. As a consequence, the elastic recovery was larger for the modified than for the original contact models, especially when the maximal plastic overlap was based on the BCC lattice. Comparing the simulations using the various contact models demonstrated the ability of the proposed model to simulate the elastic deformation of the compact.

For the modified contact models, the normal force increases rapidly with particle deformation once the maximal plastic overlap has been reached (Fig. 4a). For the BCC arrangement, the maximal plastic overlap was small, thus resulting in an early initiation of elastic deformation,

which in turn produced an extensive elastic recovery (dotted line in Fig. 4b). For the SC arrangement, with a larger maximal plastic overlap, the magnitude of the elastic recovery was comparable to the one obtained in a DEM simulation by Martin [37]. Maximal plastic overlaps based on the SC lattice were therefore regarded as more suitable and henceforth used in the numerical analysis. However, a perfect correspondence to the experimental unloading stage was not expected due to the absence of cohesion in the numerical model.

The maximal particle overlap (see Sec. 3.3) is displayed in Fig. 5. The rapid change in slope (indicated by the first set of vertical lines) represents the point at which the maximal plastic overlap was first reached for one particle contact; at this point the majority of particles are thus still deforming plastically. As several particles continuously reach the maximal plastic overlap, a network of elastically deforming particles through the compact is generated and the compact will start to deform elastically. This point may be indicated by the additional change in slope (displayed by the second set of vertical lines), which is visible for all granules at an engineering strain of about 0.35. The transition from linearity to non-linearity in Fig. 4b confirms the initiation of the elastic deformation of the compact (data for C200 and C500 not shown).

As the DEM continuously provide information about the contact behaviour, the contact evolution may easily be followed. During the rearrangement stage of the compression, the granules moved freely in the die and hence a low coordination number was displayed (data not shown). As the particle motion was reduced at increasing compression pressure the coordination number rapidly increased to a value slightly lower than 6, signifying the emergence of a confined/jammed state. During the following compression process, the coordination number increased slowly in a nearly linear manner (Fig. 6) up to a maximum of approximately 10 for both C200 and C350. The

coordination number was however somewhat lower for C500 compared to the small and intermediate sized granules. This finding is likely related to edge effects: Since the total granule mass was kept constant, the number of granules was considerably smaller for the large C500 granules, and hence a larger proportion of the granules was located at the boundary where they were in contact with fewer neighbours than the ones in the interior of the granule bed. The contact development at load was in concordance to a previous study using the original contact model [16].

The granule bed compression profiles (Fig. 7a) and the corresponding Kawakita plots (Fig. 7b) demonstrated similar compression behaviour for all granules. However, an effect of particle size was observed where the initial compressibility tended to increase with increasing particle size. This behaviour was not seen for the experimental systems, for which the compression curves were nearly equal for all sizes (compare with the experimental results in Fig. 3). This discrepancy most likely originated from the usage of the experimentally determined yield pressures in the simulations (Table 2), which decreased with increasing particle size. To see how the yield pressure is expected to affect the initial compressibility, one may idealise the agglomerate bed as a set of straight load-bearing particle columns. When compression is uniaxial, the particle overlap may be expressed as $\delta_n = 2RC$, where R is the particle radius and C is the engineering strain, as before. Provided that δ_n is much larger than δ_y, the force required to compress each column may be approximated as $F_n \approx \pi P_y R^2 C$, according to Eq. (3). Each column may be considered to occupy a cross-sectional area of $4R^2$, so that the compression pressure increases linearly with engineering strain, $P \approx \pi P_y C/4$. Despite the approximations made in its derivation, this expression provides a satisfactory explanation of the size effects seen in the numerical compression profiles. This in turn indicates that yield pressures determined from unconfined single granule

compressions may not be representative for the plastic properties during confined granule bed compressions. During bulk compression the granules are influenced by neighbouring particles that possibly alter the initiation of plastic deformation. Hence, in order to obtain more representative single granule data, confined single granule compressions may be preferable. A comparison of the maximal engineering strain obtained in Fig. 7a to the extracted Kawakita parameter *a* (Table 3) indicates that further deformation would be possible at increased compression pressure. The large differences in the 1/*b* parameter for the simulation data (Table 3) may also be explained by the differences in yield pressure discussed above.

4.3 Comparison between experimental and numerical study

As stated above, the granule bed compression process may be divided into four stages, rearrangement, plastic deformation and possibly particle fracturing, elastic deformation and finally elastic recovery during unloading. The various stages were observed from the experimental granule bed compression data (solid line in Fig. 8). During rearrangement, the granule bed was high and the particles do not experience any significant pressure. As the particles settled, the second stage was plastic deformation that is observed by the linear region of the curve. As the particles continuously deformed, forming nonporous particles, further plastic deformation is not feasible resulting in the initiation of elastic deformation. At this point, the curve started to deviate from linearity and the pressure increased rapidly. Note that some granules were still deforming plastically at this stage but transited into elastic deformation as the pressure increased, eventually giving rise to elastic deformation of the entire compact. During the unloading, a small elastic recovery of the compact is observed from the increased granule bed height. Distinct limits between the various compression stages are however difficult to detect as the transit between plastic and elastic deformation is gradual.

Simulations using the original contact model clearly resemble the first two stages of the granule bed compression process (dashed line in Fig. 8). The particle rearrangement proceeded however to a granule bed height slightly lower than for MCC granules before initiation of plastic deformation. The plastic deformation continues indefinitely until a compact height corresponding to experimental compacts was reached. The last stage of compaction was in fair agreement with experimental data with a slightly higher elastic recovery. Although the original model did not describe the complete compression process in this work, it has proven successful e.g. for prediction of Heckel parameters at low compression pressures [17] and confined compressions of alumina powder [16]. However, in the latter case, interparticle friction and yield pressure were continuously adapted to improve the correspondence to experimental data.

Simulations with the modified contact model (dotted line in Fig. 8) improved the agreement with the experimental data. As for the original model the particle rearrangement and plastic deformation was consistent for these simulations. At a granule bed height of approximately 4.2 mm the particles started to deform elastically as observed from the deviation in linearity. The elastic deformation was however not in perfect agreement with the corresponding experimental results that displayed a larger and more rapidly increasing pressure. This discrepancy may also be seen in the Kawakita a and $1/b$ parameters that are significantly larger for the simulations than for the experiments. In addition, the elastic recovery at unloading was larger than for the experiments.

In summary, the inclusion of a maximal plastic overlap in the truncated Hertzian contact model proved suitable to describe the interparticle forces during high density compression simulations.

Although the model is modified, little complexity is added and the straightforward simulation procedure is thus maintained including no prolongation in CPU-time.

The proposed modification may be improved in various ways. The most straightforward option would be to let the contact curvature $1/R_p$ decrease more rapidly with overlap than for the original truncated Hertzian model, so that larger elastic forces would be obtained. A somewhat more natural modification would be to use the bulk modulus (rather than the Young's modulus) to describe the volume change after the maximal plastic overlap has been reached. Finally, Voronoi cells may be utilized to estimate particle volumes, resulting in a model similar to the one proposed by Harthong et al. [13]. This would however increase the complexity of the DEM and particle number reduction might be necessary to maintain the computational cost within reasonable limits.

5. Conclusion

In the current work, granule bed compressions were studied both experimentally and numerically with the DEM. The parameters particle size, density, and yield pressure were measured and utilized in the simulations in order to match the experimental conditions. The frequently used truncated Hertzian model describing particle contacts for elastic-perfectly plastic materials in the DEM was modified in an attempt to enable simulation of granule bed compressions at high relative density. The new model satisfactorily described the elastic compact deformation, which previously has not been possible using a DEM contact law. The correspondence to experimental data was clearly improved but not perfect as the pressure increase was lower and less rapid for the simulated system. Despite this discrepancy, the novel model is considered promising and may

be used as a basis for further improvements. For future developments, Voronoi cells might be an interesting concept for investigations of granule bed compression at high relative density but may require a reduced size of the simulated system. In addition, confined single granule compressions may be preferable to obtain representative parameter values for simulations of confined granule bed compression.

Acknowledgements

Financial support provided by the Swedish Research Council (Project No. 621-2007-3854) is gratefully acknowledged.

Appendix

The effective radius R_* is defined as

$$\frac{1}{R_*} = \frac{1}{R_1} + \frac{1}{R_2}$$

where R_1 and R_2 are the radii of the contacting particles. For contact between a particle and a wall with negligible curvature, the reduced radius equals the particle radius. The effective Young's modulus E_* is defined as

$$\frac{1}{E_*} = \frac{1-\nu_1^2}{E_1} + \frac{1-\nu_2^2}{E_2}$$

where E_1 and E_2 (ν_1 and ν_2) are the Young's moduli (Poisson ratios) of the contacting particles. For contact with a rigid wall, only the term corresponding to the particle needs to be taken into account, since the Young's modulus of the wall tends to infinity. Similarly, the reduced shear modulus G_* is defined as

$$\frac{1}{G_*} = \frac{2-\nu_1}{G_1} + \frac{2-\nu_2}{G_2}$$

where G_1 and G_2 are the shear moduli of the contacting particles. Again, for contact with a rigid wall, only the term corresponding to the particle needs to be taken into account, since the shear modulus of the wall tends to infinity.

References

[1] P.J. James. Particle deformation during cold isostatic pressing of metal powders, Powder Metall. 20 (1977) 199-204.

[2] B. Johansson, G. Alderborn. Degree of pellet deformation during compaction and its relationship to the tensile strength of tablets formed of microcrystalline cellulose pellets, International Journal of Pharmaceutics 132 (1996) 207-220.

[3] C.Q. Sun, D.J.W. Grant. Influence of elastic deformation of particles on Heckel analysis, Pharm. Dev. Technol. 6 (2001) 193-200.

[4] A. Michrafy, D. Ringenbacher, P. Tchoreloff. Modelling the compaction behaviour of powders: application to pharmaceutical powders, Powder Technol. 127 (2002) 257-266.

[5] I.C. Sinka, J.C. Cunningham, A. Zavaliangos. The effect of wall friction in the compaction of pharmaceutical tablets with curved faces: a validation study of the Drucker-Prager Cap model, Powder Technol. 133 (2003) 33-43.

[6] C.Y. Wu, O.M. Ruddy, A.C. Bentham, B.C. Hancock, S.M. Best, J.A. Elliott. Modelling the mechanical behaviour of pharmaceutical powders during compaction, Powder Technol. 152 (2005) 107-117.

[7] G. Frenning. Analysis of pharmaceutical powder compaction using multiplicative hyperelasto-plastic theory, Powder Technol. 172 (2007) 103-112.

[8] P.A. Cundall, O.D.L. Strack. A discrete numerical model for granular assemblies, Géotechnique 29 (1979) 47-65.

[9] O. Skrinjar, P.L. Larsson. Cold compaction of composite powders with size ratio, Acta Mater. 52 (2004) 1871-1884.

[10] O. Skrinjar, P.L. Larsson. On discrete element modelling of compaction of powders with size ratio, Comp. Mater. Sci. 31 (2004) 131-146.

[11] O. Skrinjar, P.L. Larsson. On the local contact behaviour in regular lattices of composite powders, J. Mater. Process. Technol. 184 (2007) 312-318.

[12] G. Frenning. Compression mechanics of granule beds: A combined finite/discrete element study, Chem. Eng. Sci. 65 (2010) 2464-2471.

[13] B. Harthong, J.F. Jerier, P. Doremus, D. Imbault, F.V. Donze. Modeling of high-density compaction of granular materials by the Discrete Element Method, Int. J. Solids Struct. 46 (2009) 3357-3364.

[14] C.L. Martin, D. Bouvard, S. Shima. Study of particle rearrangement during powder compaction by the Discrete Element Method, J. Mech. Phys. Solids 51 (2003) 667-693.
[15] C.L. Martin, D. Bouvard. Study of the cold compaction of composite powders by the discrete element method, Acta Mater. 51 (2003) 373-386.
[16] Y. Sheng, C.J. Lawrence, B.J. Briscoe, C. Thornton. Numerical studies of uniaxial powder compaction process by 3D DEM, Eng. Computation. 21 (2004) 304-317.
[17] A. Hassanpour, M. Ghadiri. Distinct element analysis and experimental evaluation of the Heckel analysis of bulk powder compression, Powder Technol. 141 (2004) 251-261.
[18] A. Samimi, A. Hassanpour, A. Ghadiri. Single and bulk compressions of soft granules: Experimental study and DEM evaluation, Chem. Eng. Sci. 60 (2005) 3993-4004.
[19] C. Thornton, K.K. Yin. Impact of elastic spheres with and without adhesion, Powder Technol. 65 (1991) 153-166.
[20] C. Thornton, Z.M. Ning. A theoretical model for the stick/bounce behaviour of adhesive, elastic-plastic spheres, Powder Technol. 99 (1998) 154-162.
[21] B. Storåkers, S. Biwa, P.-L. Larsson. Similarity analysis of inelastic contact, Int. J. Solids Struct. 34 (1997) 3061-3083.
[22] G.D. Scott, D.M. Kilgour. Density of random close packing of spheres, J. Phys. D Appl. Phys. 2 (1969) 863-866.
[23] G. Frenning, F. Mahmoodi, J. Nordstrom, G. Alderborn. An effective-medium analysis of confined compression of granular materials, Powder Technol. 194 (2009) 228-232.
[24] A. Di Renzo, F.P. Di Maio. Comparison of contact-force models for the simulation of collisions in DEM-based granular flow codes, Chem. Eng. Sci. 59 (2004) 525-541.
[25] Y.C. Zhou, B.D. Wright, R.Y. Yang, B.H. Xu, A.B. Yu. Rolling friction in the dynamic simulation of sandpile formation, Physica A 269 (1999) 536-553.
[26] M.D. Abramoff, P.J. Magelhaes, S.J. Ram. Image Processing with ImageJ, Biophoton. Int. 11 (2004) 36-42.
[27] European Pharmacopoeia 7th Edition. *Monograph 2.9.34. Bulk and tapped density of powders*. Strasbourg: Directorate for the Quality of Medicines of the Council of Europe 2010.
[28] M. Eriksson, C. Nyström, G. Alderborn. The use of air permeametry for the assessment of external surface area and sphericity of pelletized granules, Int. J. Pharm. 99 (1993) 197-207.
[29] M. Wikberg, G. Alderborn. Compression characteristics of granulated materials II. Evaluation of granule fragmentation during compression by tablet permeability and porosity measurements, International Journal of Pharmaceutics 62 (1990) 229-241.
[30] J. Nordström, K. Welch, G. Frenning, G. Alderborn. On the physical interpretation of the Kawakita and Adams parameters derived from confined compression of granular solids, Powder Technol. 182 (2008) 424-435.
[31] K. Kawakita, K.-H. Lüdde. Some considerations on powder compression equations, Powder Technol. 4 (1971) 61-68.

[32] R.C. Rowe, R.J. Roberts, Mechanical properties, in: Alderborn G, Nystrom C, (Eds.), Pharmaceutical Powder Compaction Technology, Marcel Deeker, New York, 1996, pp. 283-322.
[33] A.-S. Persson, G. Alderborn, G. Frenning. Flowability of surface modified pharmaceutical granules: A comparative experimental and numerical study, Eur. J. Pharm. Sci. 42 (2011) 199-209.
[34] C. Sun, D.J.W. Grant. Effects of initial particle size on the tableting properties of -lysine monohydrochloride dihydrate powder, Int. J. Pharm. 215 (2001) 221-228.
[35] R.W. Heckel. Density-pressure relationships in powder compaction, T. Metall. Soc. AIME 221 (1961) 671-675.
[36] J.M. Sonnergaard. Investigation of a new mathematical model for compression of pharmaceutical powders, Eur. J. Pharm. Sci. 14 (2001) 149-157.
[37] C.L. Martin. Unloading of powder compacts and their resulting tensile strength, Acta Mater. 51 (2003) 4589-4602.

Figures and tables

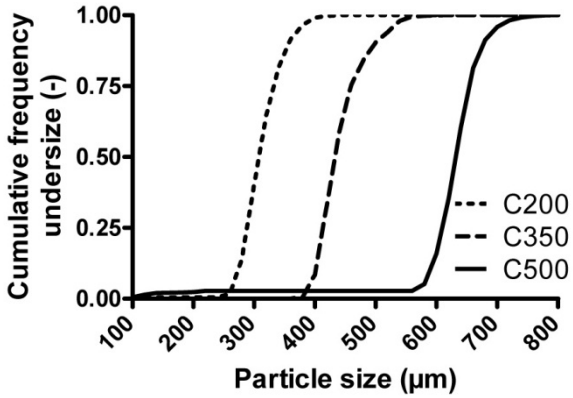

Fig. 1: Particle size distributions for C200, C350, and C500.

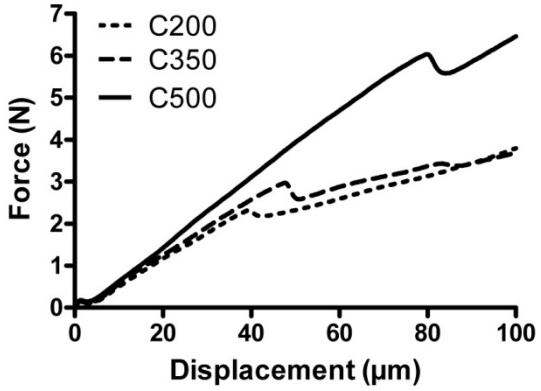

Fig. 2: Examples of force-displacement curves for single granules. Typical decreases in load, as indicated by the distinct drop in force, are observed for all granules.

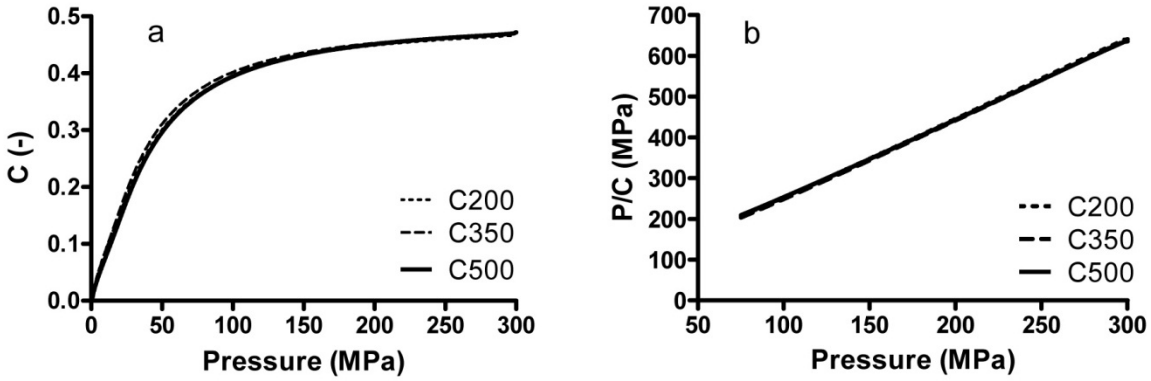

Fig. 3: Compression profiles (a) and corresponding Kawakita plots (b) for experimental bulk compressions of C200, C350, and C500.

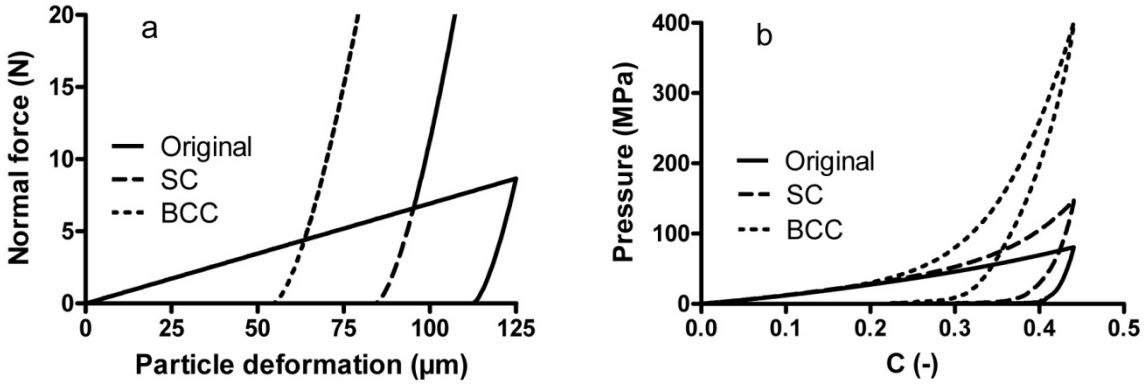

Fig. 4: Typical force-deformation curves for single granules (a) and loading-unloading curves (b) for simulated compressions of C350 using the original and modified truncated Hertzian contact model for simple-cubic (SC) and body-centred cubic lattices (BCC).

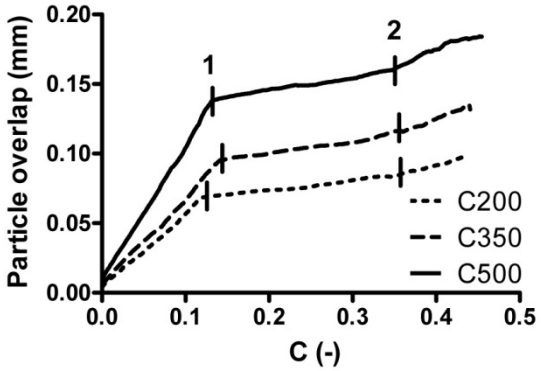

Fig. 5: Representative curves of maximal particle overlap as a function of engineering strain for simulated compressions of C200, C350, and C500. The vertical lines indicate the transitions from plastic to elastic deformation at particle contact (1) and for the compact (2).

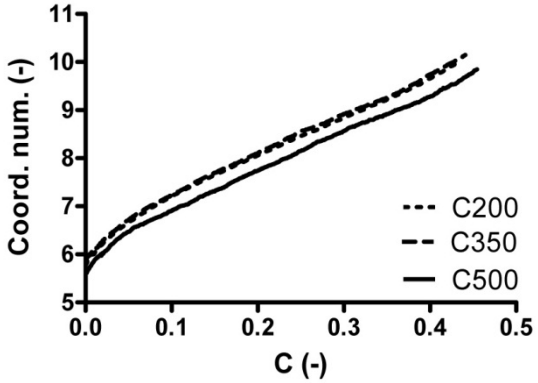

Fig. 6: Coordination number as a function of engineering strain for simulated compressions of C200, C350, and C500.

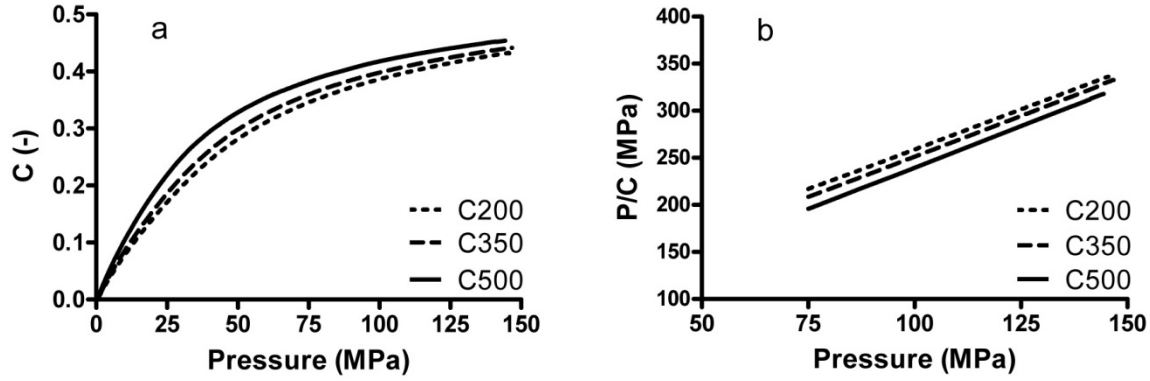

Fig. 7: Compression profiles (a) and corresponding Kawakita plots (b) for simulated compressions of C200, C350, and C500 using the modified contact model.

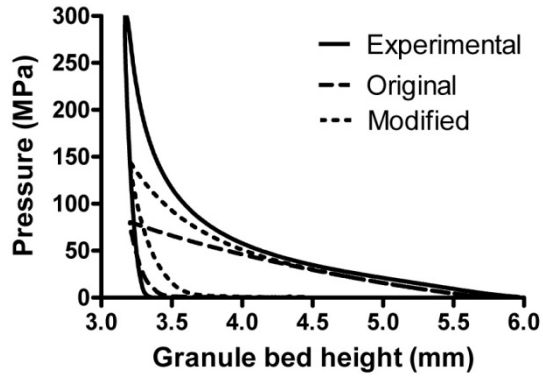

Fig. 8: Pressure as a function of granule bed height for experimental and simulated compressions of C350 using the original and modified truncated Hertzian contact model.

Table 1: Granule characteristics. Standard deviations are given in parenthesis.

	d[a] (µm)	ρ_{bulk}[b] (g/cm^3)	ρ_{tap}[c] (g/cm^3)	ρ_{eff}[d] (g/cm^3)	Porosity[e] (%)	S_A[f] (cm^{-1})
C200	317.2 (-)	0.83 (0.01)	0.92 (0.00)	1.46 (0.029)	7.3 (1.85)	268.8 (1.4)
C350	442.8 (-)	0.84 (0.01)	0.92 (0.01)	1.45 (0.005)	7.8 (0.29)	190.3 (3.1)
C500	641.3 (-)	0.89 (0.00)	0.93 (0.00)	1.44 (0.001)	8.5 (0.05)	97.1 (0.6)

[a] Median diameter.
[b] Poured bulk density (n=3).
[c] Tapped bulk density obtained after 1250 taps (n=3).
[d] Effective particle density (n=2).
[e] Calculated as 1-(ρ_{eff}/ρ_{app}).
[f] Volume specific external surface area (n=3).

Table 2: Mechanical properties of single granules. Standard deviations are given in parenthesis.

	σ_0 [a] (MPa)	P_y [b] (MPa)	E_*^c [c] (GPa)
C200	24.57 (3.95)	214.01 (36.38)	2.31 (0.33)
C350	23.33 (5.52)	199.65 (26.80)	2.56 (0.49)
C500	22.36 (3.47)	170.40 (18.31)	2.45 (0.31)

[a] Granule strength (n=50).
[b] Yield pressure (n=50).
[c] Young's modulus (n=50).

Table 3: Kawakita parameters derived from experimental and theoretical data using the modified contact model. Standard deviations are given in parenthesis.

	Experimental		Theoretical	
	a [a] (-)	$1/b$ [b] (MPa)	a [a] (-)	$1/b$ [b] (MPa)
C200	0.516 (0.004)	30.38 (0.55)	0.591 (0.001)	53.00 (0.19)
C350	0.515 (0.002)	28.18 (0.39)	0.580 (0.004)	45.68 (0.68)
C500	0.524 (0.004)	32.84 (0.80)	0.568 (0.002)	36.15 (0.68)

[a] Kawakita constant related to initial bed porosity (n=5).
[b] Kawakita constant (n=5).